RAA 2018 Vol. **18** No. **7**, 80(10pp) doi: 10.1088/1674–4527/18/7/80
© 2018 National Astronomical Observatories, CAS and IOP Publishing Ltd.
http://www.raa-journal.org *http://iopscience.iop.org/raa*

***R**esearch in*
***A**stronomy and*
***A**strophysics*

The magnification invariant of circularly-symmetric lens models

Cheng-Liang Wei[1,2], Zhe Chu[1,3] and Yi-Ping Shu[1,3]

[1] Purple Mountain Observatory, the Partner Group of MPI für Astronomie, Nanjing 210033, China; *chengliangwei@pmo.ac.cn*
[2] University of Chinese Academy of Sciences, Beijing 100049, China
[3] School of Astronomy and Space Sciences, University of Science and Technology of China, Hefei 230029, China

Received 2018 February 8; accepted 2018 April 9

Abstract In the context of strong gravitational lensing, the magnification of an image is crucially important for constraining various lens models. For several commonly used quadruple lens models, the magnification invariants, defined as the sum of the signed magnifications of images, have been analytically derived when the image multiplicity is a maximum. In this paper, we further study the magnification of several disk lens models, including (a) exponential disk lens, (b) Gaussian disk lens, (c) modified Hubble profile lens, and another two of the popular three-dimensional symmetrical lens models, (d) NFW lens and (e) Einasto lens. We find that magnification invariant exists for each lens model. Moreover, our results show that magnification invariants can be significantly changed by the characteristic surface mass density $\kappa_{\rm c}$.

Key words: gravitational lensing: strong — methods: numerical

1 INTRODUCTION

As one of the promising ways to explore cosmological information, strong gravitational lensing has been investigated in many astrophysical studies (e.g., Paraficz 2009; Cao et al. 2015; McKean et al. 2015; Yuan & Wg 2015): for determining the mass density profile of galaxies (e.g., Koopmans et al. 2009; Vegetti et al. 2012; Shu et al. 2016, 2017), measuring the masses of central black holes in distant quiescent galaxies (e.g., Mao et al. 2001; Rusin et al. 2005) and estimating the Hubble constant using time delays between multiple images in observed lensing systems (e.g., Biggs et al. 1999; Fassnacht et al. 2002; Tortora 2007; Linder 2011; Suyu et al. 2014).

In the context of strong gravitational lensing, multiple images of a given background source can be produced when the lensing system has a good alignment between the observer, lens and source (Burke 1981; Dyer & Roeder 1980; Meylan et al. 2006). Based on the magnification theorem, the total number of images of a lens is odd if the lens has a smooth surface mass density. On the other hand, gravitational lensing is able to magnify the apparent brightness of the source (Schneider et al. 1992). Thus the connection between magnification and multiple images is crucial in a variety of studies on gravitational lensing (Witt & Mao 2000; Aazami & Petters 2009; Werner 2009; Petters & Werner 2010; Tsukamoto & Harada 2013; Chu et al. 2015). For example, the summation of the image magnification for a point lens and singular isothermal sphere (SIS) lens is 1 and 2 respectively, regardless of the source positions or how large the Einstein radii are. Dalal (1998) found that the summation of signed magnifications of all the images ($I = \Sigma_i \mu_i$, where μ_i denotes the signed magnification of the $i^{\rm th}$ image) is a constant for several quadrupole lens models when the number of images is a maximum. Conventionally, this constant (I) is dubbed 'magnification invariant.' Chu et al. (2015) studied several lens models, including (1) singular isothermal elliptical density (SIED), (2) singular isothermal elliptical potential (SIEP), (3) singular isothermal quadrupole (SIQ), (4) SIS + external shear and (5) point + external shear lenses. The magnification invariants for these models are shown in Table 1. It is found that the invariant is independent of most of the model parameters, as long as the source lies inside of the caustic.

If the surface mass density of a lens is circularly symmetric, the lensing properties, such as deflection an-

Table 1 Magnification Invariants for Some Four-image Lens Models[a]

Lens model	Lens potential ψ	I^b $(=\Sigma_i\mu_i)$
1. SIED(x, y)	$x\alpha_x + y\alpha_y$	≈ 2.8
2. SIEP(x, y)	$b\sqrt{q^2x^2+y^2}$	2
3. SIQ(θ, ϕ)	$\theta_{\rm E}\theta - \frac{1}{3}\theta_{\rm E}k\theta\cos 2\phi$	1
4. SIS+shear(θ, ϕ)	$\theta_{\rm E}\theta - \frac{\gamma}{2}\theta^2\cos 2\phi$	$2/(1-\gamma^2)$
5. point+shear(θ, ϕ)	$\theta_{\rm E}^2\ln\theta - \frac{\gamma}{2}\theta^2\cos 2\phi$	$1/(1-\gamma^2)$

Notes: [a] Here b is a constant parameter, q is the axial ratio in the SIEP lens, $\theta_{\rm E}$ is the Einstein radius, $k(0 \leq k \leq 1)$ is the intensity of the quadrupole relative to the monopole in the SIQ lens and γ indicates the external shear (Chu et al. (2015); [b] Dalal (1998); Dalal & Rabin (2001); Witt & Mao (2000)). The three references in Notes[b] related to all the values of I.

gle and lensing shear, can be derived analytically, but it is not clear whether a magnification invariant can be found in the circularly-symmetric lens system (hereafter circular lens). In this paper, we study the magnification invariant of a circular lens by considering several commonly used lens models, like exponential disk lens and Gaussian disk lens. Moreover, as found in the numerical N-body simulations, the density profile of a cold dark matter halo can be described by the Navarro-Frenk-White (NFW) profile (Navarro et al. 1997). In addition, recent high-resolution simulations show that the Einasto radial profile, which is a non-singular three-parameter model, provides a more accurate description of dark matter halos (Elíasdóttir & Möller 2007; Navarro et al. 2004, 2010). For these two popular spherically symmetric density profiles, we can derive their projected surface mass density by integrating the three-dimensional (3D) density profile along the line of sight. The investigation of the magnification invariant is important to constrain these lens models.

The rest of this paper is organized as follows. In Section 2, we briefly summarize the basics of a circular lens and several commonly used lens models. In Section 3, we describe our method to derive the magnification invariants for each discussed lens model and show the dependency between derived invariants and lensing parameters. Conclusions and discussions are summarized in Section 4.

2 CIRCULAR LENS

An arbitrary surface mass density $\Sigma(\boldsymbol{\theta})$ can be expanded in terms of a complete set of orthogonal basis functions (e.g., Trotter et al. 2000), which can decompose $\Sigma(\boldsymbol{\theta})$ into multipole components,

$$\Sigma(\boldsymbol{\theta}) = \Sigma_0(\theta) + \sum_{m=1}^{\infty}\left[{\rm A}_m(\theta)\cos(m\chi) + {\rm B}_m(\theta)\sin(m\chi)\right], \tag{1}$$

where θ is the distance from the lens center and χ is the polar angle. The first term $\Sigma_0(\theta) = 1/2\pi\int_0^{2\pi}\Sigma(\boldsymbol{\theta}){\rm d}\chi$ is known as the monopole. The higher-order multipoles ($m \geqslant 1$) represent the angular structure of the mass distribution, which is composed of two parts (${\rm A}_m$ and ${\rm B}_m$). Because of the symmetry, circular lenses can be fully described by their monopole. As a kind of ideal lens model, most properties can be described analytically for a given circular lens (Miralda-Escude 1991; Schneider et al. 1992; Narayan & Bartelmann 1999). In this section, we present the basics for our analysis and also describe several commonly discussed circular lens models. Throughout the paper, we denote the observed angular position on the lens plane by $\boldsymbol{\theta} = \theta(\cos\chi, \sin\chi)$ and its source position by $\boldsymbol{\beta}$.

2.1 Basics of a Circular Lens

In general, if the mass distribution of a lens object is circularly-symmetric, the two-dimensional (2D) Poisson equation, $\nabla^2\psi(\boldsymbol{\theta}) = 2\kappa(\boldsymbol{\theta})$, can be reduced to a function only of the distance from the lens center $\theta = |\boldsymbol{\theta}|$,

$$\frac{1}{\theta}\frac{\partial}{\partial\theta}\Big(\theta\frac{\partial}{\partial\theta}\Big)\psi(\theta) = 2\kappa(\theta), \tag{2}$$

where $\psi(\theta)$ is the deflection potential and $\kappa(\theta) = \Sigma(\theta)/\Sigma_{\rm crit}$ is the dimensionless surface mass density in units of the critical surface mass density $\Sigma_{\rm crit} = {\rm c}^2D_{\rm s}/4\pi GD_{\rm d}D_{\rm ds}$. Here $D_{\rm d}$, $D_{\rm s}$ and $D_{\rm ds}$ are the angular diameter distance to the lens, to the source and between the lens and the source, respectively. For a circular lens, deflection angle $\alpha(\theta)$, lensing shear $\gamma(\theta)$ and magnification $\mu(\theta)$ are given as (Miralda-Escude 1991; Meylan et al. 2006),

$$\alpha(\theta) = \theta\bar{\kappa}(\theta), \tag{3}$$

$$\gamma(\theta) = \bar{\kappa}(\theta) - \kappa(\theta) = \frac{\alpha(\theta)}{\theta} - \kappa(\theta), \tag{4}$$

$$\frac{1}{\mu(\theta)} = \Big[1 - \frac{\alpha(\theta)}{\theta}\Big]\Big[1 + \frac{\alpha(\theta)}{\theta} - 2\kappa(\theta)\Big], \tag{5}$$

where $\bar{\kappa}(\theta) = \bar{\Sigma}(\theta)/\Sigma_{\rm crit}$ is the mean surface mass density inside θ. Since the critical curves arise at $1/\mu = 0$, Equation (5) implies that the circular lens has a pair of critical curves (Meylan et al. 2006). One, $1-\alpha(\theta)/\theta = 0$, is the tangential critical curve, which corresponds to the Einstein ring with Einstein radius. The other, $1 + \alpha(\theta)/\theta - 2\kappa(\theta) = 0$, is called the radial critical curve, which also defines a ring and the corresponding radius.

In strong gravitational lensing, multiple images can be produced for a given source. The number of images depends on the position of the source with respect to caustics, which are the mapping of the critical curves in the source plane. For circular lenses, since the tangential critical curve does not lead to a caustic curve and the corresponding caustic degenerates to a single point $\boldsymbol{\beta} = 0$, the tangential critical curve has no influence on the image multiplicity. Thus, pairs of images can only be created or destroyed if the radial critical curve exists. When a source lies inside of the radial caustic, three images will be produced at most. In general, to derive magnifications of these images, the lens equation should be solved numerically.

In the rest of this section, we will discuss several often used circular lens models, which can be analyzed analytically and are useful for theoretical investigations.

2.2 Circular Lens Models

The first lens model considered in this work is an exponential disk model, usually used to describe the mass distribution of a spiral galaxy (Lehár et al. 2000). For an exponential disk model with $\Sigma(\theta) = \Sigma_0 \exp(-\theta/\theta_0)$, convergence can be obtained as

$$\kappa_{\rm E}(\theta) = \kappa_0 \exp(-\theta/\theta_0), \tag{6}$$

where κ_0 is the central dimensionless surface mass density and θ_0 is the scale length of the lens model. The scaled deflection angle $\alpha(\theta)$ and lensing shear $\gamma(\theta)$ are derived as listed in Table 2, and these lensing properties are shown in Figure 1. Clearly, two critical curves can be identified, where $\mu(\theta) = \infty$, in the plot for magnification (the lower-right panel). Different colors indicate that the lens plane can be divided into three image regions by the two critical curves. The Fermat maximum image lies in the black line region around the center of the lens, and it has positive magnification. The minimum image arises in the blue line region, which is the outskirt of the lensing disk, and its magnification is also positive. The saddle image can be found in the red line region, which has negative magnification, and here we flip the signs in the figure. In the left panel of Figure 2, we show the distribution of the absolute value of magnification in terms of logarithm ($\log|\mu|$) in the lens plane.

Based on the lens equation, the positions of images for a given source are calculated as

$$\beta = \theta - \frac{2\kappa_0}{\theta}\Big[\theta_0^2 - \theta_0(\theta+\theta_0)\exp(-\theta/\theta_0)\Big]. \tag{7}$$

Here, the image position θ cannot be solved analytically. Thereby, it is also difficult to derive the magnifications of the three images. In this work, we use a precise numerical ray-tracing method, developed by Chu et al. (2016), to calculate the positions and corresponding magnifications of different images for a given source. The results can be found in Section 3.

We also consider another two circular lens models: The dimensionless density profile is given as $\kappa_{\rm G}(\theta) = \kappa_0 \exp(-\theta^2/\theta_0^2)$ and dubbed a Gaussian disk lens. This model can be used to describe an Einasto lens with index 1/2, as represented in Section 2.4. The other is the so-called modified Hubble profile (Rood et al. 1972), and the projected surface mass density of this lens model is defined as,

$$\Sigma(\theta) = \frac{\Sigma_0}{1+\theta^2/\theta_0^2}, \tag{8}$$

which is a softened power law lens, the dimensionless projected surface density of which can be expressed as $\kappa_{\rm MH}(\theta) = \kappa_0\theta_0^2/(\theta^2+\theta_0^2)$. For these two important lens models, their lensing properties (α, γ, and μ) are listed in Table 2.

2.3 NFW Lens

As a typical model for describing the density distribution of a dark matter halo, the NFW density profile is written as (Navarro et al. 1997; Wright & Brainerd 2000),

$$\rho(r) = \frac{\delta_{\rm c}\rho_{\rm c}}{(r/r_{\rm s})(1+r/r_{\rm s})^2}, \tag{9}$$

where $\rho_{\rm c}$ is the critical density of the universe. The scale radius, $r_{\rm s} = r_{200}/c$, is a characteristic radius of the halo, where c is the concentration parameter and the characteristic overdensity $\delta_{\rm c}$ for the halo is

$$\delta_{\rm c} = \frac{200}{3}\frac{c^2}{\ln(1+c) - c/(1+c)}. \tag{10}$$

With the thin lens approximation, we define the line of sight as the optical axis z, and the 3D NFW density profile $\rho(D_{\rm d}\boldsymbol{\theta}, z)$ will be reduced to a 2D surface mass density (e.g., Golse & Kneib 2002; Hurtado et al. 2014),

$$\Sigma(x) = \int_{-\infty}^{+\infty} \rho(x;z){\rm d}z = 2\Sigma_{\rm s}F(x). \tag{11}$$

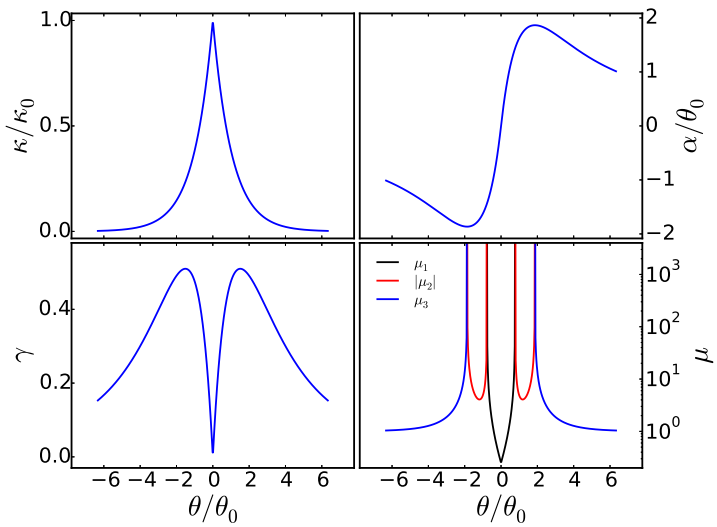

Fig. 1 The convergence $\kappa(\theta)$, deflection angle $\alpha(\theta)$, shear $\gamma(\theta)$ and magnification $\mu(\theta)$ for a typical exponential disk lens.

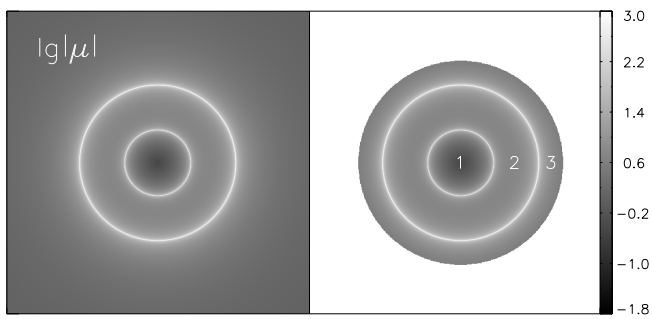

Fig. 2 The distribution of different image regions by a circularly-symmetric lens. The left panel displays the absolute value of the magnification μ in terms of logarithm. The right panel illustrates the three image regions corresponding to the source region inside of the caustic, where the gray values are derived from the left panel.

Table 2 Lens Properties of the Three Circular Lens Models

Lens model	Convergence $\kappa(\theta)$	Deflection angle $\alpha(\theta)$	Shear $\gamma(\theta)$
1. Exponential disk	$\kappa_0\exp(-\theta/\theta_0)$	$\frac{2\kappa_0}{\theta}\left[\theta_0^2-\theta_0(\theta+\theta_0)\exp(-\theta/\theta_0)\right]$	$\frac{\kappa_0}{\theta^2}\left[2\theta_0^2-(\theta^2+2\theta\theta_0+2\theta_0^2)\exp(-\theta/\theta_0)\right]$
2. Gaussian disk	$\kappa_0\exp(-\theta^2/\theta_0^2)$	$\frac{\kappa_0\theta_0^2}{\theta}\left[1-\exp(-\theta^2/\theta_0^2)\right]$	$\frac{\kappa_0}{\theta^2}\left[\theta_0^2-(\theta^2+\theta_0^2)\exp(-\theta^2/\theta_0^2)\right]$
3. Modified Hubble profile	$\kappa_0\theta_0^2/(\theta^2+\theta_0^2)$	$\frac{\kappa_0\theta_0^2}{\theta}\ln(\theta^2/\theta_0^2+1)$	$\frac{\kappa_0\theta_0^2}{\theta^2}\left[\ln(\theta^2/\theta_0^2+1)-\frac{\theta^2}{\theta^2+\theta_0^2}\right]$

Here the dimensionless radial distance $\boldsymbol{x}=\boldsymbol{\theta}/\theta_\mathrm{s}$, where $\theta_\mathrm{s}=r_\mathrm{s}/D_\mathrm{d}$. $\Sigma_\mathrm{s}=\delta_\mathrm{c}\rho_\mathrm{c}r_\mathrm{s}$ is defined as the characteristic surface mass density and the factor $F(x)$ is

$$F(x)=\begin{cases}\dfrac{1}{x^2-1}\left(1-\dfrac{1}{\sqrt{1-x^2}}\mathrm{arccosh}\dfrac{1}{x}\right) & (x<1)\\ \dfrac{1}{3} & (x=1)\\ \dfrac{1}{x^2-1}\left(1-\dfrac{1}{\sqrt{x^2-1}}\arccos\dfrac{1}{x}\right) & (x>1)\end{cases}. \tag{12}$$

Additionally, the mean surface density inside the dimensionless radius x is

$$\bar{\Sigma}(x)=\frac{1}{\pi x^2}\int_0^x 2\pi x\Sigma(x)\mathrm{d}x=4\Sigma_\mathrm{s}\frac{G(x)}{x^2}, \tag{13}$$

with

$$G(x)=\begin{cases}\ln\dfrac{x}{2}+\dfrac{1}{\sqrt{1-x^2}}\mathrm{arcch}\dfrac{1}{x} & (x<1)\\ \ln\dfrac{1}{2}+1 & (x=1)\\ \ln\dfrac{x}{2}+\dfrac{1}{\sqrt{x^2-1}}\arccos\dfrac{1}{x} & (x>1)\end{cases}. \tag{14}$$

Then the deflection angle α between the source and the image, convergence κ and shear γ can be derived,

$$\begin{cases} \alpha(x) = 4\kappa_{\rm s}\dfrac{G(x)}{x} \\ \kappa(x) = 2\kappa_{\rm s}F(x) \\ \gamma(x) = \bar{\kappa}(x) - \kappa(x) = 2\kappa_s\left(\dfrac{2G(x)}{x^2} - F(x)\right) \end{cases}. \tag{15}$$

As discussed in Bartelmann (1996), since $(\mathrm{d}\alpha/\mathrm{d}x)$ is continuous, an NFW lens can still produce three images at most, despite its central singularity.

2.4 Einasto Lens

Recent N-body simulations indicate that a non-singular three-parameter model such as the Einasto profile can provide a better description of dark matter halos in a wider range of halo mass than the NFW profile (e.g., Navarro et al. 2004, 2010; Elíasdóttir & Möller 2007; Dhar & Williams 2010; Sereno et al. 2016). The profile of an Einasto halo is (Retana-Montenegro & Frutos-Alfaro 2011)

$$\rho(r) = \rho_0 \exp\left[-\left(\frac{r}{h}\right)^{1/n}\right], \tag{16}$$

where ρ_0 is central density, h is scale length and n is Einasto index. Clearly, the Einasto profile corresponding to $n = 1$ is an exponential model in 3D and $n = 1/2$ gives a Gaussian model. With the thin lens approximation, the projected surface mass density of an Einasto lens model is derived by integrating along the line of sight of the 3D density profile as in Equation (11),

$$\Sigma(x) = \int_{-\infty}^{+\infty} \rho(x;z)\mathrm{d}z = 2\int_x^{\infty} \frac{\rho(r)r\mathrm{d}r}{\sqrt{r^2 - x^2}}, \tag{17}$$

where $r = \sqrt{x^2 + z^2}$ and we have rewritten the integration as an Abel transform (Binney & Tremaine 1987) in the right term. As studied in Retana-Montenegro et al. (2012a,b), the surface mass density of the Einasto case is derived by Mellin integral transform formalism, and related lensing properties in terms of the Fox H and Meijer G functions. More details can be referred to in Retana-Montenegro et al. (2012b).

Here, as a comparison with the exponential disk lens and Gaussian disk lens model in 2D, we will present the lensing properties for the two often used models, exponential model and Gaussian model, in 3D. Using the specific Meijer G function, we can derive the surface mass density profile and lensing properties. Table 3 provides the lensing properties for the two considered models, and it is found that the Einasto model with $n = 1/2$ can be reduced to a Gaussian disk lens model.

3 MAGNIFICATION INVARIANTS

3.1 The Test of Magnification Summation

With the purpose of calculating an accurate position of the image and its corresponding magnification for a given source, we utilize the analytical ray-tracing method in different image regions to numerically evaluate magnification for each image. This precise numerical method has been introduced in Chu et al. (2016) to study the magnification relations of quad lenses, which are shortly described as follows.

For a well-defined circular lens model, when the source lies in the radial caustic, one can find three images at most. Therefore, we pixelate the region in the radial caustic as the source area, so as to find images of it by the analytical deflection angles. As shown in Figure 2, the image of the source area can be divided into three parts in the lens plane. Each point source in the source region has three corresponding images. The saddle image lies in image region 2 with negative magnification. The other two images, lying in image regions 1 and 3, arise at the maxima and minima respectively of the time delay surface, and hence they have positive magnification.

For the sake of calculating the magnifications of the three images for a given point source $\mathcal{P}$ inside of the caustic, we need to obtain the exact positions of the three images in the lens plane. At first, we set a bundle of light rays from the observer to grids in image region 1, and then the deflected light rays will be traced back to the source region. Clearly, the image position of the source $\mathcal{P}$ can be approximately estimated by the nearest light ray to the given point source. Starting from this approximate position for the image, we are able to calculate the image positions accurately for each point source in the source region by using the Newton-Raphson method.

After deriving the positions of the images and their magnifications μ for the given lens model, we can map the divided image regions in the right panel of Figure 2 to the source plane, and estimate the magnification summation for each source. Using this numerical method, images can be matched to their source precisely in a different image region.

For the exponential disk lens, we have analytically derived the scaled deflection angle α and the magnification μ from the 2D Poisson equation in Section 2.2. Employing the numerical method introduced above, we can map the magnifications of the three different regions in the right panel of Figure 2 into the source plane accurately, and the results are displayed in Figure 3.

The left panel shows magnification μ_1 of image region 1, which corresponds to the maxima of the time

Table 3 The lensing functions $\alpha(\theta)$, $\kappa(\theta)$ and $\gamma(\theta)$ for the Einasto model with $n = 1$ and $n = 1/2$. Here κ_s is the central convergence and x defines the dimensionless radius as $x = \theta/\theta_s$. $K_\nu(x)$ is the modified Bessel function of the second kind of order ν.

Einasto index n	Convergence $\kappa(x)$	Deflection angle $\alpha(x)$	Shear $\gamma(x)$
$n = 1$	$\kappa_s x K_1(x)$	$\frac{4\kappa_s}{x}\left[1 - \frac{x^2}{2}K_2(x)\right]$	$\frac{4\kappa_s}{x^2}\left[1 - \frac{x^2}{2}K_2(x) - \frac{x^3}{4}K_1(x)\right]$
$n = 1/2$	$\kappa_s \exp(-x^2)$	$\frac{\kappa_s}{x}\left[1 - \exp(-x^2)\right]$	$\frac{\kappa_s}{x^2}\left[1 - \left(1 + x^2\right)\exp(-x^2)\right]$

delay surface and is generally demagnified. The middle panel presents images that arise at the saddle points of the time delay surface with negative magnification μ_2. Here we flipped the sign of the magnification. The magnification μ_3 of image region 3, which arises at the minima of the time delay surface, is shown in the right panel.

With these image magnifications in different image regions shown in Figure 3, we calculate the magnification summation by $\Sigma_i \mu_i = \mu_1 + \mu_2 + \mu_3$, and the result is displayed in the left panel of Figure 4 by black dots. Here the source position β has been normalized by the radial caustic $\beta_{\rm caus}$, and the error bars are estimated from the different radial bins. Note that the large error around the center happens because the magnification changes fast with an increase in radius. For arbitrary source positions within the caustic for a given set of κ_0 and θ_0, the summed magnification is almost constant, but with a subtle change, and can be evaluated by the mean value as 0.75 ± 0.03 here.

Analogous to an exponential disk lens model, we also calculate magnification summation for a Gaussian model and modified Hubble profile lens model as shown in the left panel of Figure 4, and in the right panel we show the magnification summations for the NFW lens and Einasto lens. We find the magnification summations are almost constant for these lens models, regardless of the position for the source in the radial caustic.

3.2 Dependence of Invariants on the Model Parameters

In general, for a two-parameter circular lens model, its dimensionless surface mass density can be generally defined by the characteristic surface mass density $\kappa_{\rm c}$ and the radial distribution function $f(\theta/\theta_{\rm c})$,

$$\kappa(\theta) = \kappa_{\rm c} f(\theta/\theta_{\rm c}), \tag{18}$$

where $\kappa_{\rm c}$ can be κ_0 in the disk lens model or $\kappa_{\rm s}$ in the NFW and Einasto lens models and $\theta_{\rm c}$ is the characteristic radius of the lens model, such as θ_0 in exponential disk lens model and $\theta_{\rm s}$ in NFW and Einasto lens models. If a dimensionless radial distance $x = \theta/\theta_{\rm c}$ is defined in these circular lens models, we find the lensing properties will not be changed. Thus the magnification invariants should not depend on the characteristic radius $\theta_{\rm c}$. For given model parameters $(\kappa_{\rm c}, \theta_{\rm c})$, the magnification invariant can be numerically estimated as represented above, but the dependency between the invariant and the model parameters is unclear. In this section, we test how the magnification invariant depends on the model parameters $\kappa_{\rm c}$ and $\theta_{\rm c}$.

We first verify the feasibility of our method for determining magnification invariant by considering the well defined lens model with the non-singular isothermal sphere, termed NIS (e.g., Kormann et al. 1994; Aubert et al. 2007), which is an isothermal sphere with small but finite core,

$$\kappa_{\rm NIS}(\theta) = \frac{\kappa_{\rm c}}{2\sqrt{\theta^2/\theta_{\rm c}^2 + 1}}\,. \tag{19}$$

For this specific model of the circular lens, one can analytically calculate the magnification summation of the three images. In Appendix A, we theoretically prove that the magnification invariant of NIS equals 2, which is a constant that does not depend on model parameters $\kappa_{\rm c}$ and $\theta_{\rm c}$. As a comparison, we estimate the magnification invariant I through our numerical method for the NIS model. The invariants are evaluated by the mean value of the magnification summation $\sum_{i=1}^{3} \mu_i$ at different source positions, as a function of different model parameters, $\kappa_{\rm c}$ and $\theta_{\rm c}$.

Figure 5(a) shows the magnification invariants with different parameters for the NIS model. Clearly, our numerical result indicates that the invariant of the NIS lens is equal to 2, and this magnification invariant is independent of model parameters, which agrees well with the prediction in Appendix A.

Using our numerical method, we investigate magnification invariants for the given lens models and show the results in Figure 5. We find that the invariants do not change for different scale length $\theta_{\rm c}$ as we expect, but the characteristic surface mass density $\kappa_{\rm c}$ can change the invariants significantly. When $\kappa_{\rm c}$ is large enough, the magnification invariants converge to 1 for both exponential disk lens and Einasto lens. Note that for the Einasto model, the index n is very important in determining the surface mass density characteristics, which determine the

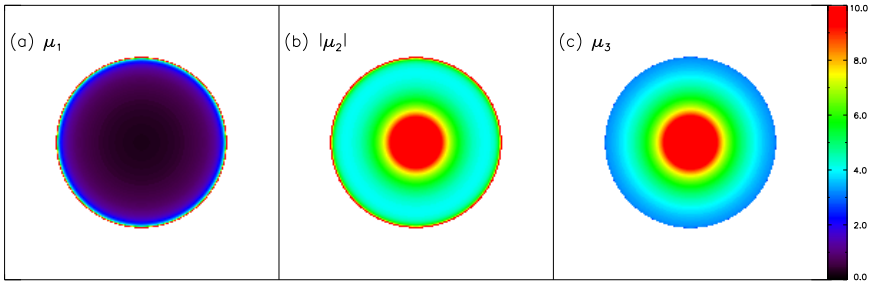

Fig. 3 The magnification distributions as functions of source positions. The values are mapped from three different image regions to source plane. The left panel shows magnification μ_1 of image region 1, which corresponds to the maxima of the time delay surface. The middle panel presents images that arise at the saddle points of the time delay surface with negative magnification μ_2, so here we flipped the sign of the magnification. The magnification μ_3 of image region 3, which arises at the minima of the time delay surface, is shown in the right panel.

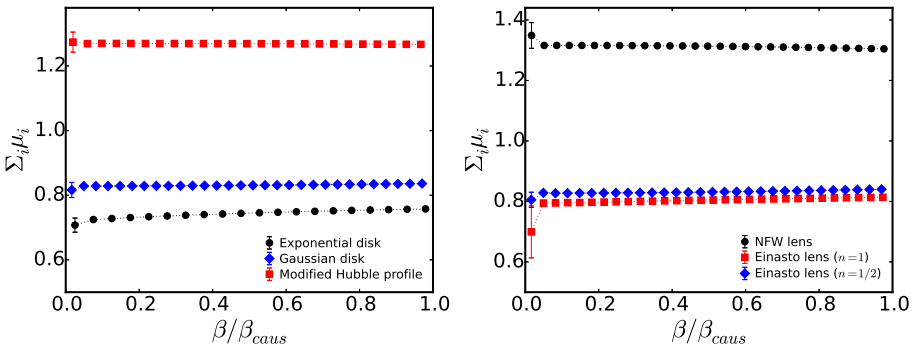

Fig. 4 The summation of signed magnifications of images for the given disk lens models is in the left panel and that for the NFW/Einasto lens models in the right panel. Source positions are scaled by the radius of radial caustic, $\beta_{\rm caus}$.

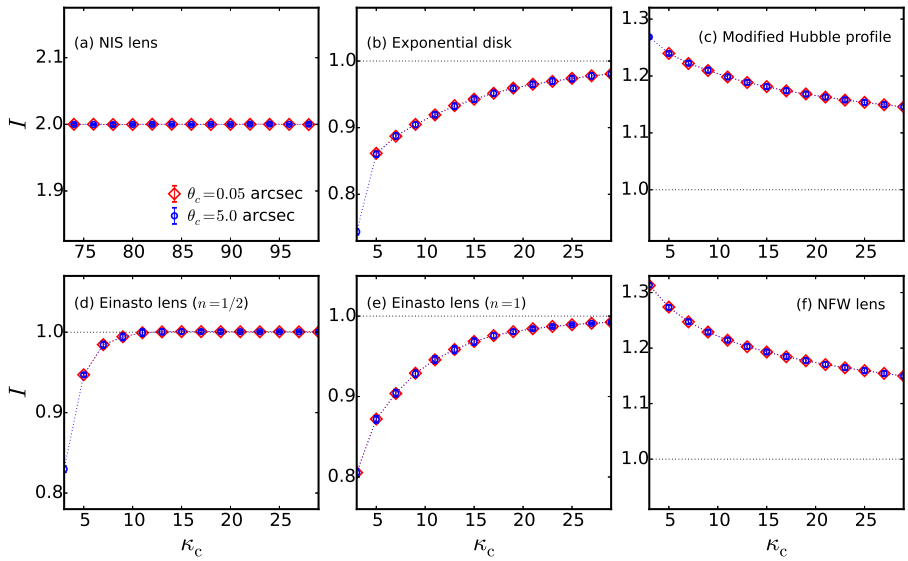

Fig. 5 The magnification invariants with the different model parameters $\kappa_{\rm c}$ and $\theta_{\rm c}$. The NIS model shows a constant magnification invariant, which is independent of model parameters, but, for the other lens models, the characteristic surface mass density $\kappa_{\rm c}$ can change the invariants significantly.

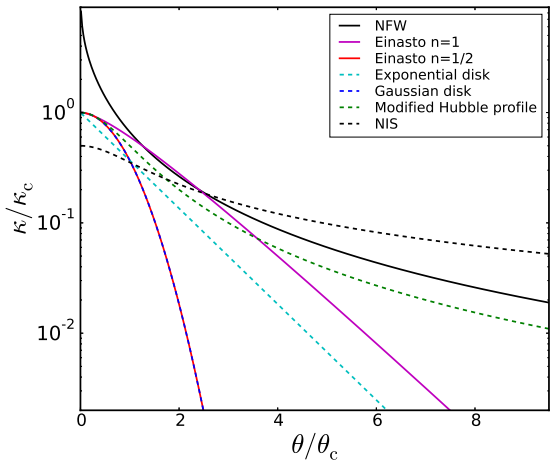

Fig. 6 Density profiles of the given lens models.

lensing properties of the respective profiles. Thus with different index n, the converged value of magnification invariants may be different. Moreover, the invariants of exponential disk lens and Einasto lens (both $n = 1/2$ and 1) increase monotonically over the characteristic surface mass density κ_c, but decrease for the modified Hubble profile and NFW lens.

This difference should result from the different density profiles of the lens models. Figure 6 shows the density profile of the applied lens models in this paper. Clearly, for the exponential disk lens and Einasto lens (both $n = 1/2$ and 1), their density profiles remarkably decrease to $\lesssim 10^{-2}\kappa_c$ at $\theta \sim 5\theta_c$. While for NFW and the modified Hubble model, the density profile decreases gradually at the outer part ($\theta > 5\theta_c$) of the lens model. For the NIS model, its density profile decreases with a more gentle slope, and this lens model gives a higher magnification invariant, which equals 2. Thus in other words, the slope of the density profile can be a potential explanation for the different converged value of magnification invariants between the different lens models. Moreover, as indicated from the density profile, the total mass is convergent for the exponential disk lens and Einasto lens, but it is divergent for the lens with modified Hubble model and NFW lens. Another potential explanation is the ratio of mass inside of the Einstein radius to the total mass, $F = M(\leq \theta_E)/M_{tot}$. We find that, for both exponential disk lens and Einasto lens ($n = 1/2$ and 1), this mass ratio tends to 1 with an increase of the characteristic surface mass density κ_c, while the mass ratio $F \to 0$ for the modified Hubble profile and NFW lens. Combining with the fact that $F = 1$ for the point lens and $F = 0$ for SIS and NIS, we speculate that when $F \to 1$ for a given lens, it will act as a point lens and have a magnification invariant of $I = 1$, but a lens with $F \to 0$, for which the total mass is not convergent, can hardly have a magnification invariant of $I \to 1$ with an increase in its model parameters. More detailed analyses in the future should be helpful for understanding the contrast between these two different results.

4 CONCLUSIONS AND DISCUSSION

Forming multiple images of a given background source is one of the most important effects of strong gravitational lensing. When the number of images is a maximum, the summation of signed magnifications of the images can be a constant for certain lens models. For some quadruple lens models, it is found that the invariant is independent of most of the model parameters, as long as the source lies inside of the caustic (Dalal 1998). In this paper, we focus on several commonly used circular lens models, in which the magnification invariants have not been investigated before. We find that for the exponential disk lens model, magnification invariant should exist, but with a very subtle change like the change of source position β in the caustic region. Moreover, we also calculate the magnifications of the other two important lens models, Gaussian disk lens and modified Hubble profile lens. Our results indicate that magnification invariants also exist for these two lens models.

Considering that the dark matter halo can be described by some universal profiles, we further examine two typical models: singular two-parameter model, e.g. NFW lens, and non-singular three-parameter model, e.g. Einasto lens. With the thin lens approximation, we find that the magnification summations of three images for an

arbitrary point source inside the caustic are constant for both the NFW and Einasto models.

More tests indicate that the magnification summation does not change with changing of the scale length $\theta_{\rm c}$, because the lensing properties will not be changed if a dimensionless radial distance $x = \theta/\theta_{\rm c}$ is defined in the circular lens models. Thus the magnification invariants are independent of the characteristic radius $\theta_{\rm c}$. However, the central density $\kappa_{\rm c}$ can affect the magnification summations significantly. In this paper, we show how the magnification summations of a given lens model vary as functions of the model parameters $\kappa_{\rm c}$ and $\theta_{\rm c}$. When $\kappa_{\rm c}$ is very large, the magnification invariant tends to be 1 for both exponential disk lens and Einasto lens (both $n = 1/2$ and 1), which can be explained in that the lens will act as a point mass with $\kappa_{\rm c}$ increasing. Moreover, the invariants of exponential disk lens and Einasto lens increase monotonically with the characteristic surface mass density $\kappa_{\rm c}$, while it is decreasing for the modified Hubble profile and NFW lens. This difference should result from the different density profiles of the lens models, and more detailed analyses should be helpful for understanding the contrast between these two different results.

Observationally, combining the magnification invariants and the measurements of Type Ia supernovae (SNe Ia), which are excellent standard candles, we can constrain the lens model in more detail, but the invariant can be significantly affected by the substructure or high-order asymmetry of lens. In the future, the magnification of a high-order lens model and of the halos in N-body simulations or hydrodynamic simulations should be studied, and the magnification invariant can be examined in a more realistic manner.

Acknowledgements The authors thank Qianli Xia for helpful discussion and suggestions. We acknowledge the supports of the National Natural Science Foundation of China (Nos. 11403103, 11603032, 11333008 and 11273061), the 973 program (Nos. 2015CB857003 and 2013CB834900), China Postdoctoral Science Foundation (2014M551681) and the Natural Science Foundation of Jiangsu Province (No. BK20140050).

Appendix A: MAGNIFICATION INVARIANT FOR NIS

As an important lens model, the SIS has been widely used in theoretical research. Another more realistic model for modeling lensing galaxies is NIS, which is profiled by an isothermal sphere with a finite core $\theta_{\rm c}$. In this case, by defining dimensionless radius $\boldsymbol{x} = \boldsymbol{\theta}/\theta_{\rm c}$, the convergence of NIS is given by

$$\kappa_{\rm NIS}(x) = \frac{\kappa_{\rm c}}{2\sqrt{x^2+1}}, \tag{A.1}$$

where $\kappa_{\rm c}$ is a constant for the given radial profile. Clearly, using the 2D Poisson equation, the lensing functions can be derived as

$$\alpha_{\rm NIS}(x) = \frac{\kappa_{\rm c}}{x}\left(\sqrt{x^2+1}-1\right), \tag{A.2}$$

$$\gamma_{\rm NIS}(x) = \frac{\kappa_{\rm c}}{x^2}\left(\sqrt{x^2+1}-1\right) - \frac{\kappa_{\rm c}}{2\sqrt{x^2+1}}. \tag{A.3}$$

Then, for a given source position y_0, combining the lens equation $y_0 = x - \alpha_{\rm NIS}(x)$ and the magnification function $1/\mu(x) = [1-\kappa_{\rm NIS}(x)]^2 - \gamma_{\rm NIS}(x)^2$, we can eliminate x and write a 3rd-degree polynomial equation in terms of μ as

$$A\mu^3 + B\mu^2 + C\mu + D = 0. \tag{A.4}$$

Here the four coefficients related to the source position y_0 and the model parameter $\kappa_{\rm c}$ are

$$\begin{cases} A = y_0^2\left[y_0^4 - y_0^2(2\kappa_{\rm c}^2+10\kappa_{\rm c}-1) + \kappa_{\rm c}(\kappa_{\rm c}-2)^3\right], \\ B = -2y_0^2\left[y_0^4 - y_0^2(2\kappa_{\rm c}^2+10\kappa_{\rm c}-1) + \kappa_{\rm c}(\kappa_{\rm c}-2)^3\right], \\ C = y_0^6 - y_0^4(3\kappa_{\rm c}^2+10\kappa_{\rm c}-1) + y_0^2\kappa_{\rm c}(3\kappa_{\rm c}^3+4\kappa_{\rm c}^2 \\ \qquad +8\kappa_{\rm c}-8) - \kappa_{\rm c}^2(\kappa_{\rm c}^2-3\kappa_{\rm c}+2)^2, \\ D = 4\kappa_{\rm c}^2\left[y_0^2 + (\kappa_{\rm c}-1)^2\right]. \end{cases}$$

Thus, we can obtain three roots at most, and these three magnifications (μ_1, μ_2, μ_3) correspond to the three images of the source at y_0 for the given NIS parameter $\kappa_{\rm c}$. As described by Vieta's formulas in mathematics, we are able to calculate the sum of these magnifications by

$$\sum_{i=1}^{3}\mu_i = -\frac{B}{A} = 2. \tag{A.5}$$

Therefore, one can formally prove that the magnification invariant is $I = \sum_i \mu_i = 2$ for the NIS lens model, providing that the source is inside the caustic. Moreover, this invariant is independent of the parameters y_0 and $\kappa_{\rm c}$.

References

Aazami, A. B., & Petters, A. O. 2009, Journal of Mathematical Physics, 50, 032501

Aubert, D., Amara, A., & Metcalf, R. B. 2007, MNRAS, 376, 113

Bartelmann, M. 1996, A&A, 313, 697

Biggs, A. D., Browne, I. W. A., Helbig, P., et al. 1999, MNRAS, 304, 349

Binney, J., & Tremaine, S. 1987, Galactic Dynamics (Princeton: Princeton Univ. Press)
Burke, W. L. 1981, ApJ, 244, L1
Cao, S., Biesiada, M., Gavazzi, R., Piórkowska, A., & Zhu, Z.-H. 2015, ApJ, 806, 185
Chu, Z., Li, G. L., & Lin, W. P. 2015, MNRAS, 449, 2079
Chu, Z., Li, G. L., Lin, W. P., & Pan, H. X. 2016, MNRAS, 461, 4466
Dalal, N. 1998, ApJ, 509, L13
Dalal, N., & Rabin, J. M. 2001, Journal of Mathematical Physics, 42, 1818
Dhar, B. K., & Williams, L. L. R. 2010, MNRAS, 405, 340
Dyer, C. C., & Roeder, R. C. 1980, ApJ, 238, L67
Elíasdóttir, Á., & Möller, O. 2007, J. Cosmol. Astropart. Phys., 7, 006
Fassnacht, C. D., Xanthopoulos, E., Koopmans, L. V. E., & Rusin, D. 2002, ApJ, 581, 823
Golse, G., & Kneib, J.-P. 2002, A&A, 390, 821
Hurtado, R., Castañeda, L., & Tejeiro, J. M. 2014, International Journal of Astronomy and Astrophysics, 4, 340
Koopmans, L. V. E., Bolton, A., Treu, T., et al. 2009, ApJ, 703, L51
Kormann, R., Schneider, P., & Bartelmann, M. 1994, A&A, 284, 285
Lehár, J., Falco, E. E., Kochanek, C. S., et al. 2000, ApJ, 536, 584
Linder, E. V. 2011, Phys. Rev. D, 84, 123529
Mao, S., Witt, H. J., & Koopmans, L. V. E. 2001, MNRAS, 323, 301
McKean, J., Jackson, N., Vegetti, S., et al. 2015, Advancing Astrophysics with the Square Kilometre Array (AASKA14), 84
Meylan, G., Jetzer, P., North, P., et al., eds. 2006, Gravitational Lensing: Strong, Weak and Micro (Berlin: Springer)
Miralda-Escude, J. 1991, ApJ, 370, 1
Narayan, R., & Bartelmann, M. 1999, in Formation of Structure in the Universe, ed. A. Dekel & J. P. Ostriker, 360
Navarro, J. F., Frenk, C. S., & White, S. D. M. 1997, ApJ, 490, 493
Navarro, J. F., Hayashi, E., Power, C., et al. 2004, MNRAS, 349, 1039
Navarro, J. F., Ludlow, A., Springel, V., et al. 2010, MNRAS, 402, 21
Paraficz, D. 2009, Cosmological Applications of Strong Gravitational Lensing, PhD thesis, Dark Cosmology Centre, Niels Bohr Institute Faculty of Science, University of Copenhagen
Petters, A. O., & Werner, M. C. 2010, General Relativity and Gravitation, 42, 2011
Retana-Montenegro, E., & Frutos-Alfaro, F. 2011, arXiv:1108.4905
Retana-Montenegro, E., Frutos-Alfaro, F., & Baes, M. 2012a, A&A, 546, A32
Retana-Montenegro, E., van Hese, E., Gentile, G., Baes, M., & Frutos-Alfaro, F. 2012b, A&A, 540, A70
Rood, H. J., Page, T. L., Kintner, E. C., & King, I. R. 1972, ApJ, 175, 627
Rusin, D., Keeton, C. R., & Winn, J. N. 2005, ApJ, 627, L93
Schneider, P., Ehlers, J., & Falco, E. E. 1992, Gravitational Lenses (Berlin: Springer-Verlag), 112
Sereno, M., Fedeli, C., & Moscardini, L. 2016, J. Cosmol. Astropart. Phys., 1, 042
Shu, Y., Bolton, A. S., Mao, S., et al. 2016, ApJ, 833, 264
Shu, Y., Brownstein, J. R., Bolton, A. S., et al. 2017, ApJ, 851, 48
Suyu, S. H., Treu, T., Hilbert, S., et al. 2014, ApJ, 788, L35
Tortora, C. 2007, in 1st Workshop of Astronomy and Astrophysics for Students, ed. N. R. Napolitano & M. Paolillo, 127
Trotter, C. S., Winn, J. N., & Hewitt, J. N. 2000, ApJ, 535, 671
Tsukamoto, N., & Harada, T. 2013, Phys. Rev. D, 87, 024024
Vegetti, S., Lagattuta, D. J., McKean, J. P., et al. 2012, Nature, 481, 341
Werner, M. C. 2009, Journal of Mathematical Physics, 50, 082504
Witt, H. J., & Mao, S. 2000, MNRAS, 311, 689
Wright, C. O., & Brainerd, T. G. 2000, ApJ, 534, 34
Yuan, C. C., & Wang, F. Y. 2015, MNRAS, 452, 2423